# Laser fluence tunable spin transport and ultrafast demagnetization in BiSbTe$_{1.5}$Se$_{1.5}$/Co$_{20}$Fe$_{60}$B$_{20}$ bilayers

Suchetana Mukhopadhyay,[1,2] Pratap Kumar Pal,[1] Subhadip Manna,[2] Chiranjib Mitra,[2] and Anjan Barman [1,*]

[1]*Department of Condensed Matter and Materials Physics, S.N. Bose National Center for Basic Sciences, Block-JD, Sector III, Salt Lake, Kolkata 700106, India*

[2]*Department of Physical Sciences, Indian Institute of Science Education and Research, Mohanpur, West Bengal 741252, India*

Topological insulator (TI)/ferromagnet heterostructures hold immense application potential for spin-orbitronic memory technologies owing to strong spin-orbit coupling of TIs combined with ultrahigh spin-charge interconversion efficiency. Here, we use all-optical time-resolved magneto-optical Kerr effect magnetometry to demonstrate fluence-modulated spin pumping and ultrafast demagnetization in Sub/BiSbTe$_{1.5}$Se$_{1.5}$(BSTS)/Co$_{20}$Fe$_{60}$B$_{20}$(CoFeB)/SiO$_2$ thin films. The effective spin-mixing conductance of the BSTS/CoFeB interface is extracted, and the two-magnon scattering (TMS) effect is isolated to reveal the true spin-pumping contribution to the damping enhancement at various laser pump fluences. The demagnetization time and Gilbert damping are found to be inversely correlated in BSTS/CoFeB due to spin-pumping-driven pure spin-current transport and interfacial spin accumulations. The fluence-dependent enhancement of spin pumping at the BSTS/CoFeB interface, surpassing TMS losses, reveals enhanced spin absorption at higher pump fluences, resulting in a factor-of-two enhancement of the spin-mixing conductance. This systematic study of femtosecond to nanosecond magnetization dynamics and pump-fluence-tunable spin pumping in a BSTS/CoFeB heterostructure can aid in the functionalization of TI-based spin-orbitronic devices and the integration of topological spintronics with femtomagnetism.

## I. INTRODUCTION

The success of spintronics, using the spin degree of freedom of the electron to implement low-energy information processing and memory technologies, is critically limited by the speed and efficiency at which magnetization can be manipulated [1]. A large body of modern spintronics research is devoted to the generation, control, and detection of high-fidelity, dissipationless pure spin currents, which promise more reliable, faster, and low-energy magnetization switching. So-called spin-orbitronic memory devices seek to utilize the strong spin-orbit coupling (SOC) in certain materials to generate spin currents and spin torques as opposed to electrical generation of spin polarization, promising enhanced durability and further miniaturization of nonvolatile memory architectures [2]. Topological spintronics seeks to utilize topological states of matter to realize energy-efficient applications. Topological states of matter are attractive because they are unusually robust and can persist without being destroyed even in the presence of small perturbations to the system [3]. Among the various classes of materials which can harbor topological states, topological insulators (TIs) form a paradigmatic realization of topological states in condensed matter experiments and have been a subject of emerging interest. Semiconducting in the bulk and possessing a bulk band gap, these materials have linearly dispersing metallic surface states maintained by time-reversal symmetry [4–6]. Time-

reversal symmetry protects surface carriers from localization by electron-electron interactions or scattering by nonmagnetic impurities or defects, promoting long spin-coherence lengths [7,8] and the possibility of long-distance, low-dissipation transport in projected device applications [9]. Additionally, the TI surface allows for more effective spin generation than a regular Rashba-coupled two-dimensional (2D) electron gas [10,11] and can provide for large charge-to-spin conversion [12,13], efficient spin filtering [14], and spin-current detection [15,16]. The strong SOC in TIs, large enough to result in band inversions in the bulk, motivated investigations aimed at harnessing the resulting large spin-orbit torque effects when coupled to an adjacent ferromagnet (FM) [12]. Although the exact manner in which magnetic films alter the topological band structure is still a subject of debate, the gapless topological surface states have been shown to persist in their presence, allowing for prospective functionalization of the surface states in TI/FM heterostructures in topological spintronics technologies [17,18]. Various spin-orbit effects such as the spin Hall effect [19], the inverse spin Hall effect [15], spin pumping [20,21], the Rashba effect [22], the inverse Rashba-Edelstein effect, and the anomalous Hall effect [23] have already been observed in TI/FM systems. Of these, the spin-pumping phenomenon is particularly attractive as a sensitive probe for spin injection and transport in TIs, being free of the impedance mismatch problem [24], and provides an efficient means for the generation of pure spin currents without the requirement of a bias charge current. Here, the precessing effective magnetization of a FM material acts as a source of spin accumulation at its interface with another

*abarman@bose.res.in
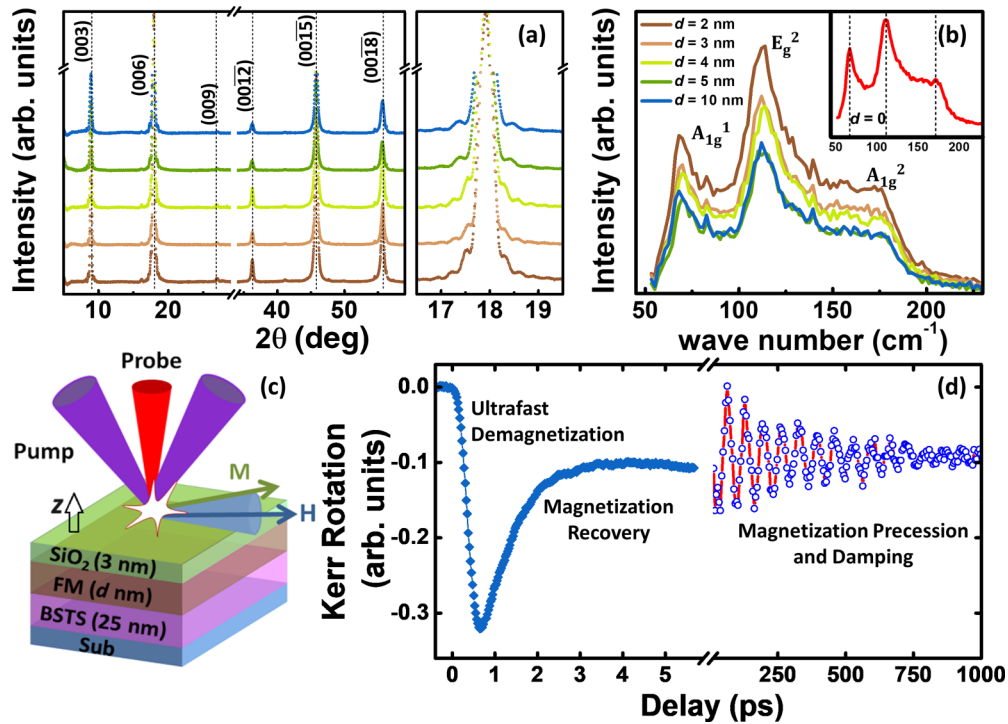
FIG. 1. (a) X-Ray diffraction pattern for BSTS (25 nm)/CoFeB($d$) samples. The right panel shows Laue oscillations near the (0, 0, 6) peak. (b) Micro-Raman spectrum for BSTS (25 nm)/CoFeB($d$) samples as well as for a 25 nm BSTS thin film indicating the characteristic modes. (c) A schematic of the BSTS/CoFeB samples with pump-probe measurement geometry. (d) Typical time-resolved magneto-optical Kerr effect (TRMOKE) data showing temporal evolution of magnetization.

material. If the FM is interfaced with a high SOC nonmagnetic material, the latter can act as a spin sink, providing channels for dissipating the interfacial spin accumulation. This loss of spin angular momentum from the precessing magnetization of the FM due to pure spin-current transport across the nonmagnet/FM interface manifests as an enhancement in the Gilbert damping factor of the FM and can be detected by electrical or optical means.

So far, electrical detection of spin injection and transport [15,20,21] or magnetoresistance measurements [25,26] have formed the basis of most reports of spin-to-charge interconversion mechanisms in TI/FM heterostructures. Reports of the spin-pumping effect have mostly relied on spin-torque FM resonance (ST-FMR) measurements [15,27]. In contrast with these electrical detection techniques, an all-optical pump-probe technique, time-resolved magneto-optical Kerr effect (TRMOKE) magnetometry [28], offers a noninvasive all-optical detection scheme free from any complicated microfabrication requirements, employing femtosecond laser pulses both for the excitation of magnetization dynamics in a system and for probing it locally [29,30]. Moreover, TRMOKE offers a laser-pulsewidth-limited temporal resolution, which makes it ideal for the simultaneous investigation and correlation of the subpicosecond optical spin-manipulation processes such as ultrafast demagnetization [31] and the nanosecond magnetization precession and damping. Motivated by the lack of studies on picosecond ultrafast demagnetization and its correlation with Gilbert damping in the presence of spin pumping in TI/FM heterostructures, we carried out an all-optical investigation of laser pump-fluence-modulated picosecond to

nanosecond magnetization dynamics in heterostructures of the quarternary TI $BiSbTe_{1.5}Se_{1.5}$ (BSTS) with amorphous $Co_{20}Fe_{60}B_{20}$ (CoFeB). BSTS has been identified to have a near-ideal bulk insulating property [26] and has among the lowest reported defect densities for specific compositions [32–34], making it an ideal system for realizing the unique advantages of TIs [35–37]. We have measured and characterized both the laser-induced ultrafast demagnetization and magnetic damping in BSTS/CoFeB bilayers at various pump fluences using the TRMOKE technique. By studying the modulation of Gilbert damping as a function of CoFeB thickness, we have extracted the effective spin-mixing conductance $G_{\text{eff}}$ which characterizes the efficiency of spin pumping at the BSTS/CoFeB interface and isolated the role of the two-magnon scattering (TMS) effect in the observed damping modulation. The effect of BSTS on the magnetization dynamics has been underpinned by contrasting the results with those obtained in reference CoFeB thin films without a BSTS underlayer. Further, we have correlated the Gilbert damping with the ultrafast demagnetization process to reveal that interfacial spin accumulations parameterized by the spin chemical potential largely influence the ultrafast demagnetization in our system. The pump fluence is found to effectively enhance the spin-pumping effect and lead to enhanced spin absorption and lowering of interfacial spin accumulations at higher fluences.

## II. RESULTS AND DISCUSSION

Since chalcogenides are prone to react with neighboring transition metals, we first sought to confirm that the structural properties of the bilayers are as expected. Results of

x-ray diffraction (XRD) and micro-Raman measurements carried out on the BSTS (25 nm)/CoFeB($d$) heterostructures ($d = 2-5$ and 10 nm) are shown in Figs. 1(a) and 1(b). The presence of characteristic XRD peaks at $(0, 0, 3n)$ indices in all the BSTS/CoFeB bilayer samples as well as the persistence of Laue oscillations informs us that the structural integrity and crystalline quality of BSTS is well preserved after deposition of the magnetic CoFeB film. Similarly, characteristic Raman modes were observed at 67.97, 112.03, and 172.27 $cm^{-1}$, designated as $A_{1g}^1$, $E_g^2$, and $A_{1g}^2$ modes, respectively, in all the bilayer samples as well as a bare 25 nm BSTS film [38].

Subsequently, time-resolved measurements of laser-induced magnetization dynamics were carried out using a custom-built two-color TRMOKE technique using a non-collinear measurement geometry, as shown in Fig. 1(c) [30] (see Supplemental Material [38] for details). A typical TRMOKE trace showing the evolution of the local magnetization over the picosecond-to-nanosecond time domain is shown in Fig. 1(d). The picosecond time regime in this figure shows the signature ultrafast demagnetization phenomenon [31], in which interaction of a femtosecond laser with a FM leads to a rapid quenching of its magnetization. In transition metal FMs and alloys at room temperature and under low-to-moderate-fluence laser excitation, the demagnetization generally occurs over a period of a few hundred femtoseconds and is followed by a slower, two-step recovery over a few tens to hundreds of picoseconds [39]. At a microscopic level, the ultrafast magnetization quenching is variously attributed to coherent interaction of spins with laser field [40], local spin-flip scattering processes mediated by electrons [41] and magnons [42], impurity- and defect-mediated Elliot-Yafet scattering [39], or nonlocal transport processes such as laser-induced ultrafast superdiffusive spin transport [43]. On the other hand, a macroscopic, thermal description of the demagnetization process is commonly adopted in the literature, which describes the demagnetization process in terms of thermal exchange between the electron, lattice, and spin subsystems in the excited magnetic material, while making no presumptions about the details of the underlying microscopic mechanisms [31]. From this three-temperature picture, by considering electron and lattice specific heats constant and neglecting spin specific heat and electron thermalization time, the following analytical expression can be derived for the magnetization evolution [44]:

$$-\frac{\Delta M_z}{M_z} = \left[ \left\{ \frac{A_1}{\left(1 + \frac{t}{\tau_0}\right)^{1/2}} - \frac{(A_2\tau_E - A_1\tau_M)\exp\left(-\frac{t}{\tau_M}\right)}{\tau_E - \tau_M} \right. \right.$$
$$\left. \left. - \frac{\tau_E(A_1 - A_2)\exp\left(-\frac{t}{\tau_E}\right)}{\tau_E - \tau_M} \right\} \Theta(t) + A_3\delta(t) \right] * \gamma(t),$$
$$(1)$$

where $*$ denotes the convolution product, $\gamma(t)$ is the Gaussian laser pulse, $\delta(t)$ is the Dirac delta function, and $\Theta(t)$ is the step function. The amplitude $A_1$ represents the value of the normalized magnetization after demagnetization has completed and equilibrium between the electron, lattice, and spin systems been reestablished; $A_2$ is proportional to the initial electron temperature rise and thus also to the maximum magnetization

quenching; while $A_3$ represents the magnitude of state-filling effects present during the onset of demagnetization. The state-filling or bleaching effects are eliminated in a two-color pump-probe experiment and are not relevant in the fitting. The time constants $\tau_0$, $\tau_M$, and $\tau_R$ represent the heat diffusion time scale, the demagnetization time, and fast magnetization recovery time, respectively. In our experiments, we used TRMOKE magnetometry to measure the ultrafast demagnetization in the BSTS (25 nm)/CoFeB($d$) samples, followed by the coherent magnetization precession superposed on the slow magnetization recovery. The experimental demagnetization traces are fitted to Eq. (1) to extract $\tau_M$. Prior to the fit, all the traces are normalized by the value of total Kerr rotation signal under the saturating magnetic field in the absence of laser excitation. Figures 2(a) and 2(b) show the experimentally obtained ultrafast demagnetization traces for a set of reference CoFeB($d$) and BSTS (25 nm)/CoFeB($d$) samples, respectively, from which the faster demagnetization in the latter set is readily apparent. To quantify this change, the values of $\tau_M$ for each sample series extracted from the fits with Eq. (1) are shown in Fig. 2(c). Here, $\tau_M$ is much less in the presence of a BSTS underlayer, serving as the first indication that BSTS acts as a spin sink, facilitating spin transport and reducing $\tau_M$. Moreover, $\tau_M$ is found to increase with CoFeB thickness $d$ in the presence of a BSTS underlayer, while in its absence, it is relatively uncorrelated with $d$. Figures 3(a) and 3(b) show the ultrafast demagnetization traces at different pump fluences for BSTS/CoFeB (2 nm) and BSTS/CoFeB (5 nm) thin films, from which an increase in $\tau_M$ with increase of fluence is apparent. This effect can be attributed to enhanced spin-fluctuations at elevated spin temperatures for higher fluences [45,46].

To investigate whether the spin-sink nature of BSTS is responsible for the accelerated demagnetization in the presence of a BSTS underlayer, we investigated the precessional magnetization dynamics for both the CoFeB($d$) and BSTS (25 nm)/CoFeB($d$) sample series, as shown in Figs. 2(d) and 2(e). In the presence of a magnetic field, the magnetization dynamics of a FM system is governed by the dual action of the Landau-Lifshitz torque which leads to the precession of the magnetization direction around the effective field direction and the material-specific intrinsic Gilbert damping, which results in the decay of the precessional oscillations to a time-independent equilibrium magnetization direction. On the other hand, gyromagnetic precession in the FM can generate a nonequilibrium spin accumulation at its interface with an adjacent nonmagnet [47], acting as a spin source or generator. If the interfacing nonmagnetic material has high SOC, it can act as a sink for the dissipation of spin-angular momentum from the precessing magnetization in the FM, which manifests in an enhancement of the effective damping [47–49]. In the presence of the spin pumping, the Landau-Lifshitz-Gilbert equation is modified by an additive component, according to [48,49]

$$\frac{d\mathbf{m}}{dt} = -\gamma(\mathbf{m} \times \mathbf{H}_{\text{eff}}) + \alpha_0\left(\mathbf{m} \times \frac{d\mathbf{m}}{dt}\right) + \frac{\gamma}{VM_s}I_0$$
$$= -\gamma(\mathbf{m} \times \mathbf{H}_{\text{eff}}) + \left(\alpha_0 + \frac{\gamma\hbar G_{\text{eff}}}{4\pi VM_s}\right)\left(\mathbf{m} \times \frac{d\mathbf{m}}{dt}\right),$$
$$(2)$$
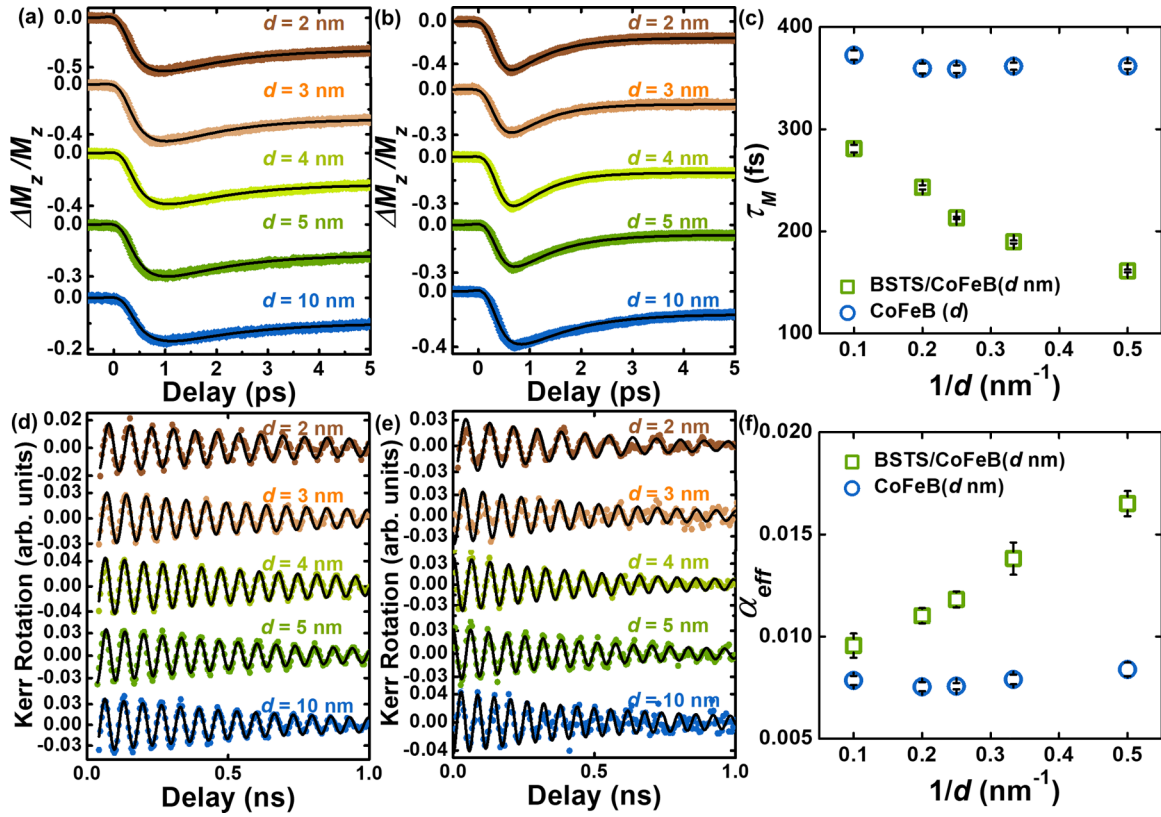
FIG. 2. (a) Ultrafast demagnetization traces for CoFeB($d$) and (b) BSTS (25 nm)/CoFeB($d$) samples under pump fluence 10.3 mJ cm$^{-2}$. Solid lines are fits to Eq. (1). (c) Variation of demagnetization time $\tau_M$ as a function of $d$ with and without BSTS underlayer. (d) Precessional Kerr rotation data for CoFeB($d$) and (e) BSTS (25 nm)/CoFeB($d$) samples at an external field of 1.9 kOe and pump fluence 10.3 mJ cm$^{-2}$. Solid lines are fits to a damped sinusoidal function [38]. (f) Modulation of damping constant $\alpha_{\text{eff}}$ with $d$ with and without BSTS underlayer.

where $\gamma$ is the gyromagnetic ratio, $H_{\text{eff}}$ is the effective magnetic field, $\alpha_0$ is the intrinsic Gilbert damping of the FM, while $V$ and $M_s$ denote its volume and its saturation magnetization, respectively. The total pumped current $I_0$ is the sum of the forward spin current $I_{\text{pump}}$ pumped into the nonmagnetic layer and the backflow current $I_{\text{back}}$ which returns to the FM. The material-specific effective spin-mixing conductance $G_{\text{eff}}$ [50] of the FM/nonmagnet interface acts as a measure of the net transfer of spin-angular momentum and self-consistently accounts for the spin backflow, thus quantifying the efficiency of spin pumping in a given nonmagnet/FM system. The value of $G_{\text{eff}}$ governs the modulation of damping by the thickness of the FM layer $d$ according to the functional relationship [29,49]:

$$\alpha_{\text{eff}} = \alpha_0 + \frac{g\mu_B}{4\pi M_s d} G_{\text{eff}}. \tag{3}$$

In the presence of interfacial defects and inhomogeneities, the TMS effect leads to the scattering of the uniform FMR mode into degenerate magnons [51,52], which can disproportionately enhance damping at lower FM thicknesses. TMS arises due to a combination of interfacial SOC and magnetic roughness at the interface [16,53,54]. In the presence of both spin pumping and TMS, the total damping modulation can be expressed as [55,56]

$$\alpha_{\text{eff}} = \alpha_0 + \frac{g\mu_B}{4\pi M_s d} G_{\text{eff}} + \frac{\beta_{\text{TMS}}}{d^2}. \tag{4}$$

The precessional data taken at 1.9 kOe saturating field for BSTS (25 nm)/CoFeB($d$) are given in Fig. 2(e). The effective Gilbert damping parameter $\alpha_{\text{eff}}$ for a sample can be extracted using its effective saturation magnetization $M_{\text{eff}}$ and the decay time $\tau$ of observed precessional oscillations as $\alpha_{\text{eff}} = 1/[\gamma_0\tau(H + 2\pi M_{\text{eff}})]$. For our films, sources of inhomogeneous broadening apart from TMS were effectively ruled out (see Ref. [38] for details). Here, $\alpha_{\text{eff}}$ is found to show a sharp increase with the inverse of CoFeB layer thickness $d$, consistent with the presence of a strong spin-pumping effect in our systems. The observed dependence is fitted with the sum of linear and quadratic scaling with $d^{-1}$ given in Eq. (4), arising from spin-pumping and TMS effects, respectively. From the fit, a high effective spin-mixing conductance of $G_{\text{eff}} = (1.19 \pm 0.024) \times 10^{15}$ cm$^{-2}$ was obtained while the TMS coefficient $\beta_{\text{TMS}}$ was found to be $(7.74 \pm 0.704) \times 10^{-17}$ cm$^2$ at a pump fluence of 10.3 mJ cm$^{-2}$. The value of $G_{\text{eff}}$ we obtained is of the order of values previously reported in other TI/FM systems [15,21]. In the case of TIs, the surface states can constitute an additional spin relaxation channel. The pumped spin current from the FM generates both a three-dimensional (3D) charge current in the bulk due to the inverse spin Hall effect and a 2D charge current in the topological surface states due to the inverse Edelstein effect [20,21]. While the former contribution dominates in room temperature spin-pumping experiments, charge-to-spin conversion in bulk insulating TI is significantly larger than
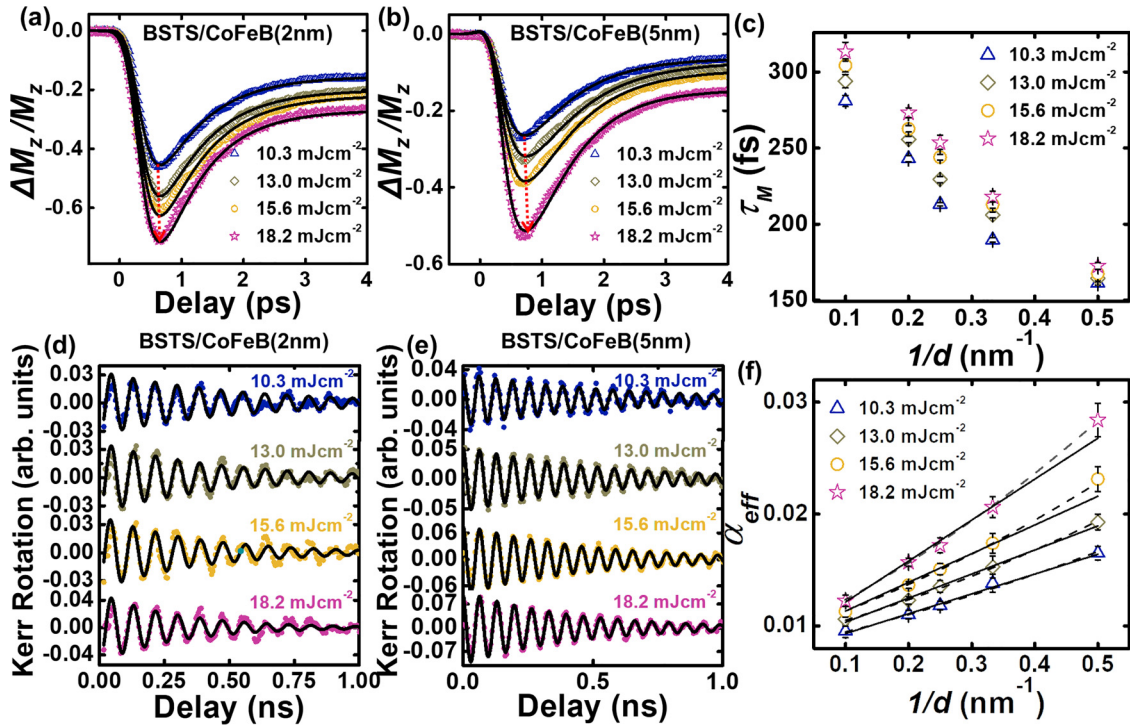
FIG. 3. (a) Ultrafast demagnetization traces for BSTS (25 nm)/CoFeB (2 nm) and (b) BSTS (25 nm)/CoFeB (5 nm) samples for various pump fluences $F$. Solid lines are fits to Eq. (1). (c) Variation of $\tau_M$ as a function of CoFeB thickness $d$ for various values of $F$. (d) Precessional Kerr rotation data for BSTS (25 nm)/CoFeB (2 nm) and (e) BSTS (25 nm)/CoFeB (5 nm) samples for various values of $F$ at an external field of 1.9 kOe. Solid lines are fits to a damped sinusoidal function [38]. (f) Modulation of damping constant $\alpha_{\mathrm{eff}}$ with $d$ as a function of $F$. Solid lines are fits to Eq. (3) and dashed lines are fits to Eq. (4).

that observed in $5d$ transition metals [57], which can explain the large $G_{\mathrm{eff}}$ values obtained in this paper. Figures 3(d) and 3(e) show the background-subtracted precessional Kerr signal for BSTS/CoFeB (2 nm) and BSTS/CoFeB (5 nm) at different pump fluences. Evidently, increase in fluence results in an enhancement of $\alpha_{\mathrm{eff}}$, but the extent of this enhancement is much more prominent in BSTS/CoFeB (2 nm) than that in BSTS/CoFeB (5 nm). The fact that the fluence dependence of $\alpha_{\mathrm{eff}}$ depends on the thickness of the CoFeB layer allowed us to ascribe it to a thickness-dependent interfacial mechanism, which could be well described by the model outlined in Eq. (4), which considers a sum of spin-pumping and TMS contributions. Figure 3(f) shows how the thickness-dependent modulation of $\alpha_{\mathrm{eff}}$ is tuned by the laser pump. Although $\alpha_{\mathrm{eff}}$ is found to increase with increase in laser fluence for all the samples, the degree of increase is higher for films with lower $d$, showing that the thickness-dependent damping modulation is dependent on the pump fluence. Fitting the data in Fig. 3(f) with Eq. (3), the spin-mixing conductance $G_{\mathrm{eff}}$ is extracted as a function of fluence, as shown in Fig. 4(a), showing a considerable fluence-dependent enhancement $(1.19 \pm 0.024) \times 10^{15}$ cm$^{-2}$ at 10.3 mJ cm$^{-2}$ to $(2.32 \pm 0.024) \times 10^{15}$ cm$^{-2}$ at 18.2 mJ cm$^{-2}$. On the other hand, increasing laser fluence can also result in a larger number of scattering events at the interface, exacerbating the dissipative effect known as spin memory loss (SML), in which the spin-pumping-induced spin transmission is reduced by spin-flip scattering events at the interface mediated by the interfacial SOC [58,59]. To verify whether the

fluence-dependent damping modulation is driven by SML, we measured precessional data after introducing a 1 nm Cu spacer layer between the BSTS and CoFeB layers as a control.
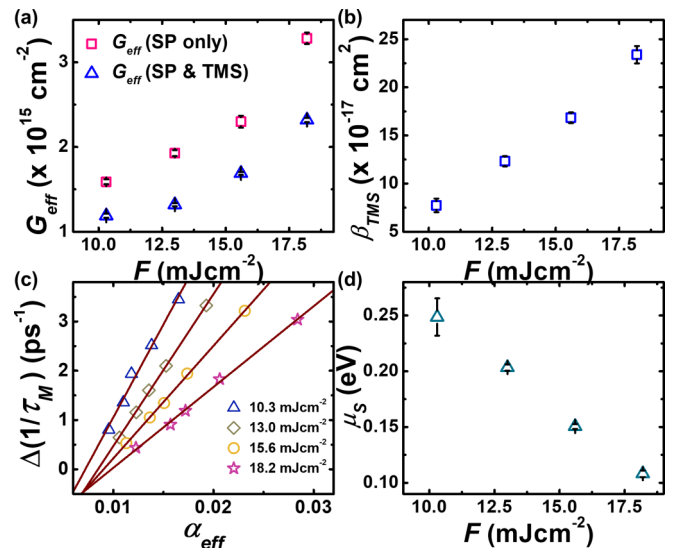


FIG. 4. (a) Variation of effective spin-mixing conductance $G_{\mathrm{eff}}$ with pump fluence $F$ by neglecting or considering two-magnon scattering (TMS) losses. (b) Enhancement of TMS coefficient $\beta_{\mathrm{TMS}}$ with increasing $F$. (c) Correlation of ultrafast demagnetization rate $\Delta(1/\tau_M)$ with Gilbert damping $\alpha_{\mathrm{eff}}$ as a function of $F$. Solid lines show fits to Eq. (5). (d) Variation of the spin chemical potential $\mu_s$ with $F$.

Cu has low spin-flip scattering probability and a very long spin-diffusion length, so SML is minimal at the Cu interfaces, while spin current generated by spin pumping transports ballistically through it. Comparative TRMOKE traces for the BSTS (25 nm)/CoFeB (5 nm) and BSTS (25 nm)/Cu (1 nm)/CoFeB (5 nm) samples are shown in Fig. S4 in the Supplemental Material [38], showing that the damping modulation is nearly identical for both samples, showing that SML has a minor role to play in the fluence dependence of damping. However, higher fluences may also lead to a more prominent interfacial TMS effect, which may contribute to the observed damping modulation. To isolate this effect, the data in Fig. 3(f) are fitted with Eq. (4), revealing a fluence-dependent enhancement of the TMS coefficient $\beta_{TMS}$, as shown in Fig. 4(b). However, even when the enhanced TMS is accounted for, $G_{eff}$ still shows a factor-of-two increment within our experimental fluence range. This fluence-dependent tunability of spin pumping provides a route for ultrafast laser control of spin current and magnetic damping in high-performance spintronics devices. The possibility of isolating the surface-state contribution to the fluence dependence of damping can be explored in future work.

Although the characteristic time scales of ultrafast demagnetization and the precessional magnetization dynamics in FM thin films differ by many orders of magnitude, several works have established that the correlation between $\tau_M$ and $\alpha_{eff}$ can shed light on the dominant microscopic mechanisms underlying the ultrafast demagnetization. In simple FM systems, an inversely proportional relationship between $\tau_M$ and $\alpha_{eff}$ was analytically derived from quantum mechanical considerations [60]; however, it failed to be experimentally validated when both $\tau_M$ and $\alpha_{eff}$ were tuned by transition metal and rare-earth doping [61]. It was later proposed that the nature of the correlation between $\tau_M$ and $\alpha_{eff}$ depends upon the major microscopic contribution to the damping. A linear relationship between $\tau_M$ and $\alpha_{eff}$ indicates a dominating conductivity-like contribution to the damping due to intraband electron and hole scattering, whereas in the presence of dominant resistivity-like damping arising from interband scattering, an inverse correlation emerges [62]. Zhang *et al.* [63] later established that the breathing Fermi surface model is valid in cases where local spin-flip scattering processes dominate the demagnetization process, predicting a proportional relationship between $\tau_M$ and $\alpha_{eff}$. On the other hand, they have been demonstrated to be inversely related to the material spin polarization at the Fermi energy [64]. Likewise, an inverse correlation between $\tau_M$ and $\alpha_{eff}$ may also arise in the presence of SOC in magnetic bilayers and multilayers. Here, nonlocal spin transport provides an additional relaxation channel, resulting in an enhancement of the magnetic damping accompanied by an acceleration of ultrafast demagnetization at the femtosecond time scale [63].

As seen in Figs. 2(c) and 2(f), for the BSTS/CoFeB bilayer system, it is observed that $\tau_M$ and $\alpha_{eff}$ are inversely correlated as a function of $d$, i.e., while $\alpha_{eff}$ increases with decreasing $d$, $\tau_M$ decreases. Since the CoFeB thickness-dependent modulation of $\alpha_{eff}$ arises from spin pumping according to Eq. (3), it can be inferred that faster demagnetization occurs at lower $d$ due to additional dissipation channels provided by the spin-current transport across the BSTS/CoFeB interface.

According to a model based on the theory of laser-induced ultrafast superdiffusive spin transport, at a particular excitation fluence, the change of the rate of ultrafast demagnetization $\Delta(1/\tau_M)$ and the modulation of Gilbert damping $\Delta\alpha$ of CoFeB in the presence of a BSTS underlayer show an approximately linear relationship, which can be fitted using the following equation [63]:

$$\Delta\frac{1}{\tau_M} = \frac{1}{\tau_M} - \frac{1}{\tau_{M[CoFeB]}} = \frac{\mu_s}{\hbar}(\alpha_{eff} - \alpha_0), \qquad (5)$$

where $\tau_M[CoFeB]$ and $\alpha_0$ are the values of demagnetization time and the intrinsic Gilbert damping factor of CoFeB in the absence of a BSTS underlayer, and $\mu_s$ is the spin chemical potential which is proportional to spin accumulations at the BSTS/CoFeB interface. According to this model, interfacial spin accumulations at the BSTS/CoFeB interface play a major role in the acceleration of ultrafast demagnetization in the CoFeB layer as well as the Gilbert damping enhancement. Taking the value of $\tau_{M[CoFeB]} = 362$ fs, $\mu_s$ is extracted for various pump fluences by fitting the curves shown in Fig. 4(c) with Eq. (5). Figure 4(d) shows the values of $\mu_s$ at various fluences, showing a 56% decrement from 248 to 108 meV within the experimental fluence range. This decrease indicates that spin-angular momentum dissipation in the ultrafast channel becomes less efficient with the increase of laser fluence due to the emergence of enhanced spin fluctuations at higher fluences [45].

## III. CONCLUSIONS

In conclusion, we used an all-optical TRMOKE technique to investigate laser-induced ultrafast demagnetization and Gilbert damping in BiSbTe$_{1.5}$Se$_{1.5}$(BSTS)/Co$_{20}$Fe$_{60}$B$_{20}$ (CoFeB) heterostructures with varying thickness $d$ of the CoFeB layer. In the presence of a BSTS underlayer, the ultrafast demagnetization time $\tau_M$ is found to increase with $d$, signaling the opening of additional relaxation channels which gain prominence as $d$ is lowered. The modulation of Gilbert damping $\alpha_{eff}$ with thickness of the CoFeB layer is characteristic of the presence of efficient spin pumping in these heterostructures and reveals that the interfacial spin-accumulation-driven spin-current transport is the origin of acceleration of the demagnetization process at lower $d$ values, where the effect of spin-current transport becomes more prominent. Thereby, an inverse relationship between $\tau_M$ and $\alpha_{eff}$ is established in these heterostructures as a function of $d$. By modeling the CoFeB-thickness-dependent variation of $\alpha_{eff}$ for various laser pump fluences, we extracted the effective spin-mixing conductance $G_{eff}$ at the interface and isolated the TMS coefficient $\beta_{TMS}$ at each pump fluence. Even when higher TMS is accounted for, increasing pump fluence leads to a factor-of-two enhancement of $G_{eff}$ within our experimental fluence range. The inverse correlation between $\tau_M$ and $\alpha_{eff}$ in BSTS/CoFeB signifies that transport of pure spin currents generated by the interfacial spin-pumping mechanism dominates the demagnetization process in these heterostructures, in agreement with the model proposed by Zhang *et al.* [63]. Our systematic study of magnetization dynamics across a wide time domain allows us to establish clear relationships between ultrafast demagnetization, Gilbert damping, and the

experimental laser pump fluence which can help in the design and implementation of pure spin-current-driven topological spintronic devices and propounds a path toward the integration of topological spintronics with femtomagnetism.

## ACKNOWLEDGMENTS

[1] A. Hirohata, K. Yamada, Y. Nakatani, I.-L. Prejbeanu, B. Diény, P. Pirro, and B. Hillebrands, Review on spintronics: Principles and device applications, J. Magn. Magn. Mater. **509**, 166711 (2020).

[2] Q. Shao, P. Li, L. Liu, H. Yang, S. Fukami, A. Razavi, H. Wu, K. Wang, F. Freimuth, Y. Mokrousov *et al.*, Roadmap of spin-orbit torques, IEEE Trans. Magn. **57**, 1 (2021).

[3] J. C. Y. Teo, L. Fu, and C. L. Kane, Surface states and topological invariants in three- dimensional topological insulators: Application to $Bi_{1-x}Sb_x$, Phys. Rev. B **78**, 045426 (2008).

[4] L. Fu, C. L. Kane, and E. J. Mele, Topological insulators in three dimensions, Phys. Rev. Lett. **98**, 106803 (2007).

[5] M. Z. Hasan and C. L. Kane, Colloquium: Topological insulators, Rev. Mod. Phys. **82**, 3045 (2010).

[6] X.-L. Qi and S.-C. Zhang, Topological insulators and superconductors, Rev. Mod. Phys. **83**, 1057 (2011).

[7] H. Zhang, C.-X. Liu, X.-L. Qi, X. Dai, Z. Fang, and S.-C. Zhang, Topological insulators in $Bi_2Se_3$, $Bi_2Te_3$ and $Sb_2Te_3$ with a single Dirac cone on the surface, Nat. Phys. **5**, 438 (2009).

[8] P. Roushan, J. Seo, C. V. Parker, Y. S. Hor, D. Hsieh, D. Qian, A. Richardella, M. Z. Hasan, R. J. Cava, and A. Yazdani, Topological surface states protected from backscattering by chiral spin texture, Nature (London) **460**, 1106 (2009).

[9] Q. L. He, T. L. Hughes, N. P. Armitage, Y. Tokura, and K. L. Wang, Topological spintronics and magnetoelectronics, Nat. Mater. **21**, 15 (2022).

[10] D. Pesin and A. H. MacDonald, Spintronics and pseudospintronics in graphene and topological insulators, Nat. Mater. **11**, 409 (2012).

[11] J. Han and L. Liu, Topological insulators for efficient spin-orbit torques, APL Mater. **9**, 060901 (2021).

[12] Y. Fan and K. L. Wang, Spintronics based on topological insulators, SPIN **06**, 1640001 (2016).

[13] H. Wang, J. Kally, J. S. Lee, T. Liu, H. Chang, D. R. Hickey, K. A. Mkhoyan, M. Wu, A. Richardella, and N. Samarth, Surface-state-dominated spin-charge current conversion in topological-insulator–ferromagnetic-insulator heterostructures, Phys. Rev. Lett. **117**, 076601 (2016).

[14] J. Wu, J. Liu, and X.-J. Liu, Topological spin texture in a quantum anomalous Hall insulator, Phys. Rev. Lett. **113**, 136403 (2014).

[15] P. Deorani, J. Son, K. Banerjee, N. Koirala, M. Brahlek, S. Oh, and H. Yang, Observation of inverse spin Hall effect in bismuth selenide, Phys. Rev. B **90**, 094403 (2014).

[16] K. Fujiwara, Y. Fukuma, J. Matsuno, H. Idzuchi, Y. Niimi, Y. Otani, and H. Takagi, 5*d* iridium oxide as a material for spin-current detection, Nat. Commun. **4**, 2893 (2013).

[17] M. R. Scholz, J. Sánchez-Barriga, D. Marchenko, A. Varykhalov, A. Volykhov, L. V. Yashina, and O. Rader, Tolerance of topological surface states towards magnetic moments: Fe on $Bi_2Se_3$, Phys. Rev. Lett. **108**, 256810 (2012).

[18] Y. Wang, P. Deorani, K. Banerjee, N. Koirala, M. Brahlek, S. Oh, and H. Yang, Topological surface states originated spin-orbit torques in $Bi_2Se_3$, Phys. Rev. Lett. **114**, 257202 (2015).

[19] A. R. Mellnik, J. S. Lee, A. Richardella, J. L. Grab, P. J. Mintun, M. H. Fischer, A. Vaezi, A. Manchon, E.-A. Kim, N. Samarth *et al.*, Spin-transfer torque generated by a topological insulator, Nature (London) **511**, 449 (2014).

[20] Y. Shiomi, K. Nomura, Y. Kajiwara, K. Eto, M. Novak, K. Segawa, Y. Ando, and E. Saitoh, Spin-electricity conversion induced by spin injection into topological insulators, Phys. Rev. Lett. **113**, 196601 (2014).

[21] M. Jamali, J. S. Lee, J. S. Jeong, F. Mahfouzi, Y. Lv, Z. Zhao, B. K. Nikolić, K. A. Mkhoyan, N. Samarth, and J.-P. Wang, Giant spin pumping and inverse spin Hall effect in the presence of surface and bulk spin-orbit coupling of topological insulator $Bi_2Se_3$, Nano Lett. **15**, 7126 (2015).

[22] Y. Lv, J. Kally, D. Zhang, J. S. Lee, M. Jamali, N. Samarth, and J.-P. Wang, Unidirectional spin-Hall and Rashba-Edelstein magnetoresistance in topological insulator-ferromagnet layer heterostructures, Nat. Commun. **9**, 111 (2018).

[23] L. D. Alegria, H. Ji, N. Yao, J. J. Clarke, R. J. Cava, and J. R. Petta, Large anomalous Hall effect in ferromagnetic insulator-topological insulator heterostructures, Appl. Phys. Lett. **105**, 053512 (2014).

[24] K. Ando, S. Takahashi, J. Ieda, H. Kurebayashi, T. Trypiniotis, C. H. W. Barnes, S. Maekawa, and E. Saitoh, Electrically tunable spin injector free from the impedance mismatch problem, Nat. Mater. **10**, 655 (2011).

[25] C. H. Li, O. M. J. van 't Erve, J. T. Robinson, Y. Liu, L. Li, and B. T. Jonker, Electrical detection of charge-current-induced spin polarization due to spin-momentum locking in $Bi_2Se_3$, Nat. Nanotechnol. **9**, 218 (2014).

[26] Y. Ando, T. Hamasaki, T. Kurokawa, K. Ichiba, F. Yang, M. Novak, S. Sasaki, K. Segawa, Y. Ando, and M. Shiraishi, Electrical detection of the spin polarization due to charge flow in the surface state of the topological insulator $Bi_{1.5}Sb_{0.5}Te_{1.7}Se_{1.3}$, Nano Lett. **14**, 6226 (2014).

[27] F. Bonell, M. Goto, G. Sauthier, J. F. Sierra, A. I. Figueroa, M. V. Costache, S. Miwa, Y. Suzuki, and S. O. Valenzuela, Control of spin-orbit torques by interface engineering in topological insulator heterostructures, Nano Lett. **20**, 5893 (2020).

[28] M. van Kampen, C. Jozsa, J. T. Kohlhepp, P. LeClair, L. Lagae, W. J. M. de Jonge, and B. Koopmans, All-optical probe of coherent spin waves, Phys. Rev. Lett. **88**, 227201 (2002).

[29] O. Mosendz, V. Vlaminck, J. E. Pearson, F. Y. Fradin, G. E. W. Bauer, S. D. Bader, and A. Hoffmann, Detection and quantification of inverse spin Hall effect from spin pumping in permalloy/normal metal bilayers, Phys. Rev. B **82**, 214403 (2010).

[30] A. Barman and J. Sinha, *Spin Dynamics and Damping in Ferromagnetic Thin Films and Nanostructures* (Springer, Cham, 2018).

[31] E. Beaurepaire, J.-C. Merle, A. Daunois, and J.-Y. Bigot, Ultrafast spin dynamics in ferromagnetic nickel, Phys. Rev. Lett. **76**, 4250 (1996).

[32] D. O. Scanlon, P. D. C. King, R. P. Singh, A. de la Torre, S. M. Walker, G. Balakrishnan, F. Baumberger, and C. R. A. Catlow, Controlling bulk conductivity in topological insulators: Key role of anti-site defects, Adv. Mater. **24**, 2154 (2012).

[33] Z. Ren, A. A. Taskin, S. Sasaki, K. Segawa, and Y. Ando, Optimizing $Bi_{2-x}Sb_xTe_{3-y}Se_y$ solid solutions to approach the intrinsic topological insulator regime, Phys. Rev. B **84**, 165311 (2011).

[34] A. Pandey, S. Singh, B. Ghosh, S. Manna, R. Gopal, and C. Mitra, Pulsed laser deposition of highly *c*-axis oriented thin films of BSTS topological insulator, arXiv:1910.08100.

[35] J. Lee, J. Park, J.-H. Lee, J. S. Kim, and H.-J. Lee, Gate-tuned differentiation of surface-conducting states in $Bi_{1.5}Sb_{0.5}Te_{1.7}Se_{1.3}$ topological-insulator thin crystals, Phys. Rev. B **86**, 245321 (2012).

[36] T. Arakane, T. Sato, S. Souma, K. Kosaka, K. Nakayama, M. Komatsu, T. Takahashi, Z. Ren, K. Segawa, and Y. Ando, Tunable Dirac cone in the topological insulator $Bi_2\text{-}xSb_xTe_3\text{-}ySe_y$, Nat. Commun. **3**, 636 (2012).

[37] Y. Xu, I. Miotkowski, C. Liu, J. Tian, H. Nam, N. Alidoust, J. Hu, C.-K. Shih, M. Z. Hasan, and Y. P. Chen, Observation of topological surface state quantum Hall effect in an intrinsic three-dimensional topological insulator, Nat. Phys. **10**, 956 (2014).

[38] See Supplemental Material at http://link.aps.org/supplemental/10.1103/PhysRevB.109.024437 for the experimental methods including PLD deposition of BSTS, details of XRD and micro-Raman characterization of BSTS, deposition of CoFeB, atomic force microscopy images of Sub/BSTS(25 nm)/CoFeB $(d)$/SiO$_2$(3 nm) heterostructures, TRMOKE measurements, detailed analysis of bias magnetic-field-dependent TRMOKE data and extraction of Gilbert damping, and comparative TRMOKE results on Sub/BSTS(25 nm)/Cu (1 nm)/CoFeB (5 nm)/SiO$_2$(3 nm) and Sub/CoFeB (5 nm)/SiO$_2$(3 nm) samples. It also contains Refs. [28,34,58,63,65–85].

[39] B. Koopmans, G. Malinowski, F. Dalla Longa, D. Steiauf, M. Fähnle, T. Roth, M. Cinchetti, and M. Aeschlimann, Explaining the paradoxical diversity of ultrafast laser- induced demagnetization, Nat. Mater. **9**, 259 (2010).

[40] J.-Y. Bigot, M. Vomir, and E. Beaurepaire, Coherent ultrafast magnetism induced by femtosecond laser pulses, Nat. Phys. **5**, 515 (2009).

[41] M. Krauß, T. Roth, S. Alebrand, D. Steil, M. Cinchetti, M. Aeschlimann, and H. C. Schneider, Ultrafast demagnetization of ferromagnetic transition metals: The role of the Coulomb interaction, Phys. Rev. B **80**, 180407(R) (2009).

[42] M. Cinchetti, M. Sánchez Albaneda, D. Hoffmann, T. Roth, J.-P. Wüstenberg, M. Krauß, O. Andreyev, H. C. Schneider, M. Bauer, and M. Aeschlimann, Spin-flip processes and ultrafast magnetization dynamics in Co: Unifying the microscopic and macroscopic view of femtosecond magnetism, Phys. Rev. Lett. **97**, 177201 (2006).

[43] M. Battiato, K. Carva, and P. M. Oppeneer, Superdiffusive spin transport as a mechanism of ultrafast demagnetization, Phys. Rev. Lett. **105**, 027203 (2010).

[44] F. Dalla Longa, J. T. Kohlhepp, W. J. M. de Jonge, and B. Koopmans, Influence of photon angular momentum on ultrafast demagnetization in nickel, Phys. Rev. B **75**, 224431 (2007).

[45] U. Atxitia, O. Chubykalo-Fesenko, J. Walowski, A. Mann, and M. Münzenberg, Evidence for thermal mechanisms in laser-induced femtosecond spin dynamics, Phys. Rev. B **81**, 174401 (2010).

[46] K. C. Kuiper, G. Malinowski, F. D. Longa, and B. Koopmans, Nonlocal ultrafast magnetization dynamics in the high fluence limit, J. Appl. Phys. **109**, 07D316 (2011).

[47] Y. Tserkovnyak, A. Brataas, and G. E. W. Bauer, Enhanced Gilbert damping in thin ferromagnetic films, Phys. Rev. Lett. **88**, 117601 (2002).

[48] Y. Tserkovnyak, A. Brataas, and G. E. W. Bauer, Spin pumping and magnetization dynamics in metallic multilayers, Phys. Rev. B **66**, 224403 (2002).

[49] Y. Tserkovnyak, A. Brataas, G. E. W. Bauer, and B. I. Halperin, Nonlocal magnetization dynamics in ferromagnetic heterostructures, Rev. Mod. Phys. **77**, 1375 (2005).

[50] A. Brataas, Y. V. Nazarov, and G. E. W. Bauer, Finite-element theory of transport in ferromagnet–normal metal systems, Phys. Rev. Lett. **84**, 2481 (2000).

[51] M. J. Hurben and C. E. Patton, Theory of two magnon scattering microwave relaxation and ferromagnetic resonance linewidth in magnetic thin films, J. Appl. Phys. **83**, 4344 (1998).

[52] R. Arias and D. L. Mills, Extrinsic contributions to the ferromagnetic resonance response of ultrathin films, Phys. Rev. B **60**, 7395 (1999).

[53] L. Zhu, Lujun Zhu, D. C. Ralph, and R. A. Buhrman, Origin of strong two-magnon scattering in heavy-metal/ferromagnet/oxide heterostructures, Phys. Rev. Appl. **13**, 034038 (2020).

[54] G. Woltersdorf and B. Heinrich, Two-magnon scattering in a self-assembled nanoscale network of misfit dislocations, Phys. Rev. B **69**, 184417 (2004).

[55] S. N. Panda, S. Majumder, S. Choudhury, A. Bhattacharya, S. Sinha, and A. Barman, Femtosecond laser-induced spin dynamics in single-layer graphene/CoFeB thin films, Nanoscale **13**, 13709 (2021).

[56] K. Dutta, S. N. Panda, T. Seki, S. Pan, K. Takanashi, and A. Barman, All-optical detection of spin pumping and giant interfacial spin transparency in $Co_2Fe_{0.4}Mn_{0.6}Si$/Pt heterostructure, Adv. Quantum Technol. **5**, 2200033 (2022).

[57] Z. Chi, Y.-C. Lau, X. Xu, T. Ohkubo, K. Hono, and M. Hayashi, The spin Hall effect of Bi-Sb alloys driven by thermally excited Dirac-like electrons, Sci. Adv. **6**, eaay2324 (2020).

[58] J.-C. Rojas-Sánchez, N. Reyren, P. Laczkowski, W. Savero, J.-P. Attané, C. Deranlot, M. Jamet, J.-M. George, L. Vila, and H. Jaffrès, Spin pumping and inverse spin Hall effect in platinum: The essential role of spin-memory loss at metallic interfaces, Phys. Rev. Lett. **112**, 106602 (2014).

[59] K. Chen, and S. Zhang, Spin pumping in the presence of spin-orbit coupling, Phys. Rev. Lett. **114**, 126602 (2015).

[60] B. Koopmans, J. J. M. Ruigrok, F. D. Longa, and W. J. M. de Jonge, Unifying ultrafast magnetization dynamics, Phys. Rev. Lett. **95**, 267207 (2005).

[61] J. Walowski, G. Müller, M. Djordjevic, M. Münzenberg, M. Kläui, C. A. F. Vaz, and J. A. C. Bland, Energy equilibration processes of electrons, magnons, and phonons at the femtosecond time scale, Phys. Rev. Lett. **101**, 237401 (2008).

[62] W. Zhang, W. He, X.-Q. Zhang, Z.-H. Cheng, J. Teng, and M. Fähnle, Unifying ultrafast demagnetization and intrinsic Gilbert damping in Co/Ni bilayers with electronic relaxation near the Fermi surface, Phys. Rev. B **96**, 220415(R) (2017).

[63] W. Zhang, Q. Liu, Z. Yuan, K. Xia, W. He, Q.-F. Zhan, X.-Q. Zhang, and Z.-H. Cheng, Enhancement of ultrafast demagnetization rate and Gilbert damping driven by femtosecond laser-induced spin currents in $Fe_{81}Ga_{19}/Ir_{20}Mn_{80}$ bilayers, Phys. Rev. B **100**, 104412 (2019).

[64] C. Guillemard, W. Zhang, G. Malinowski, C. de Melo, J. Gorchon, S. Petit-Watelot, J. Ghanbaja, S. Mangin, P. Le Fèvre, F. Bertran et al., Engineering $Co_2MnAl_xSi_{1-x}$ Heusler compounds as a model system to correlate spin polarization, intrinsic Gilbert damping, and ultrafast demagnetization, Adv. Mater. **32**, 1908357 (2020).

[65] J. Schou, Physical aspects of the pulsed laser deposition technique: The stoichiometric transfer of material from target to film, Appl. Surf. Sci. **255**, 5191 (2009).

[66] R. K. Gopal, S. Singh, A. Mandal, J. Sarkar, and C. Mitra, Topological delocalization and tuning of surface channel separation in $Bi_2Se_2Te$ topological insulator thin films, Sci. Rep. **7**, 4924 (2017).

[67] I. Garate and L. Glazman, Weak localization and antilocalization in topological insulator thin films with coherent bulk-surface coupling, Phys. Rev. B **86**, 035422 (2012).

[68] Y. Liu, M. Weinert, and L. Li, Spiral growth without dislocations: Molecular beam epitaxy of the topological insulator $Bi_2Se_3$ on epitaxial graphene/SiC(0001), Phys. Rev. Lett. **108**, 115501 (2012).

[69] P. Orgiani, C. Bigi, P. K. Das, J. Fujii, R. Ciancio, B. Gobaut, A. Galdi, C. Sacco, L. Maritato, P. Torelli et al., Structural and electronic properties of $Bi_2Se_3$ topological insulator thin films grown by pulsed laser deposition, Appl. Phys. Lett. **110**, 171601 (2017).

[70] Z. Liao, M. Brahlek, J. M. Ok, L. Nuckols, Y. Sharma, Q. Lu, Y. Zhang, and H. N. Lee, Pulsed-laser epitaxy of topological insulator $Bi_2Te_3$ thin films, APL Mater. **7**, 041101 (2019).

[71] Y. Tung, Y. F. Chiang, C. W. Chong, Z. X. Deng, Y. C. Chen, J. C. A. Huang, C.-M. Cheng, T.-W. Pi, K.-D. Tsuei, Z. Li et al., Growth and characterization of molecular beam epitaxy-grown $Bi_2Te_{3-x}Se_x$ topological insulator alloys, J. Appl. Phys. **119**, 055303 (2016).

[72] R. German, E. V. Komleva, P. Stein, V. G. Mazurenko, Z. Wang, S. V. Streltsov, Y. Ando, and P. H. M. van Loosdrecht, Phonon mode calculations and Raman spectroscopy of the bulk-insulating topological insulator $BiSbTeSe_2$, Phys. Rev. Mater. **3**, 054204 (2019).

[73] U. Mukhopadhyay, D. Chaudhuri, J. Sarkar, S. Singh, R. K. Gopal, S. Tammu, P. C. Upadhya, and C. Mitra, Surface optical and bulk acoustic phonons in the topological insulator, $Bi_2Se_2Te$, Appl. Phys. Lett. **106**, 241106 (2015).

[74] J. Yuan, M. Zhao, W. Yu, Y. Lu, C. Chen, M. Xu, S. Li, K. P. Loh, and B. Qiaoliang, Raman spectroscopy of two-dimensional $Bi_2Te_xSe_{3-x}$ platelets produced by solvothermal method, Materials **8**, 5007 (2015).

[75] C. Kittel, On the theory of ferromagnetic resonance absorption, Phys. Rev. **73**, 155 (1948).

[76] D. Givord, O. F. K. McGrath, C. Meyer, and J. Rothman, Interface magnetic anisotropy, J. Magn. Magn. Mater. **157–158**, 245 (1996).

[77] G. Wu, D. Wu, Y. Ren, Q. Y. Jin, and Z. Zhang, Topological surface state manipulation of magnetic damping and surface anisotropy in topological insulator/nonmagnet/CoFe heterostructures, Phys. Rev. B **103**, 014419 (2021).

[78] Z. Zhu, G. Wu, Y. Ren, S. Lou, Q. Y. Jin, and Z. Zhang, Modulation of magnetic damping in antiferromagnet/CoFeB heterostructures, Appl. Phys. Lett. **116**, 182407 (2020).

[79] G. Wu, Y. Ren, X. He, Y. Zhang, H. Xue, Z. Ji, Q. Y. Jin, and Z. Zhang, Tuning magnetization dynamics with strong spin-orbit coupling in transition-metal dichalcogenide/Co-Fe-B heterostructures, Phys. Rev. Appl. **13**, 024027 (2020).

[80] Y. Fan, X. Ma, F. Fang, J. Zhu, Q. Li, T. P. Ma, Y. Z. Wu, Z. H. Chen, H. B. Zhao, and G. Lüpke, Photoinduced spin angular momentum transfer into an antiferromagnetic insulator, Phys. Rev. B **89**, 094428 (2014).

[81] J. Walowski, M. Djordjevic Kaufmann, B. Lenk, C. Hamann, J. McCord, and M. Münzenberg, Intrinsic and non-local Gilbert damping in polycrystalline nickel studied by Ti : sapphire laser fs spectroscopy, J. Phys. D: Appl. Phys. **41**, 164016 (2008).

[82] H.-S. Song, K.-D. Lee, J.-W. Sohn, S.-H. Yang, S. S. P. Parkin, C.-Y. You, and S.-C. Shin, Relationship between Gilbert damping and magneto-crystalline anisotropy in a Ti-buffered Co/Ni multilayer system, Appl. Phys. Lett. **103**, 022406 (2013).

[83] D. Steiauf and M. Fähnle, Damping of spin dynamics in nanostructures: An ab initio study, Phys. Rev. B **72**, 064450 (2005).

[84] K. Gilmore, M. D. Stiles, J. Seib, D. Steiauf, and M. Fähnle, Anisotropic damping of the magnetization dynamics in Ni, Co, and Fe, Phys. Rev. B **81**, 174414 (2010).

[85] Y. Li, Y. Li, R. Sun, J.-N. Liu, N. Li, X. Yang, Z.-Z. Gong, Z.-K. Xie, W. He, and X.-Q. Zhang, Drag effect induced large anisotropic damping behavior in magnetic thin films with strong magnetic anisotropy, J. Phys.: Condens. Matter **33**, 175801 (2021).